Engineered Science
DOI: https://dx.doi.org/10.30919/es1621

Molecular Engineering of Phthalocyanine-based Azo Covalent Organic Framework Materials for Improving Lithium Storage Behaviors

Danlin Sun,[#] Suqin Liu,[#] Gaoyou Du, Qiong Luo, Renjie Peng and Jun Chen[*]

Abstract

Phthalocyanine-based polymers are promising for energy storage due to their tunable redox-active sites, robust frameworks, and conjugated properties. However, the structure-property relationship between phthalocyanine content and electrochemical performance remains unclear, hindering the rational design of high-performance electrodes. In this work, the influence of phthalocyanine content was systematically investigated by controlling the molar ratio of N,N,N',N'-tetrakis (p-aminophenyl) p-phenylenediamine (TPPDA) to tetranitro-nickel phthalocyanine (NiPc-$(NO_2)_4$) (2:1, 1:1, 1:2). Three TPPDA-NiPc azo polymers were synthesized, revealing that higher phthalocyanine content enhanced structural integrity, azo bond density, and polymerization degree, while incorporating more reversible redox sites. The TPPDA-NiPc (1:2) electrode exhibited superior cycling stability and rate capability, delivering a maximum capacity of 970.5 mAh g^{-1} at 100 mA g^{-1}f 453.6 and 238.4 mAh g^{-1} higher than the (2:1) and (1:1) electrodes, respectively. This performance stems from the optimized polymer network and shortened ion transport paths enabled by phthalocyanine incorporation.

Keywords: Lithium-ion batteries; Organic electrode; Molecular engineering; Covalent organic framework; Phthalocyanine.
Received: 06 May 2025; Revised: 18 May 2025; Accepted: 23 June 2025
Article type: Research article.

1. Introduction

The contemporary energy crisis, driven by rapid societal development and exacerbated by environmental degradation from fossil fuel combustion. This pressing situation has prompted an urgent need to develop new energy storage devices that are both effective and environmentally friendly.[1] Lithium-ion batteries (LIBs) have established themselves as the dominant energy storage technology for portable electronics and electric vehicles due to key advantages such as exceptionally high energy density and relatively low environmental impact.[2-4] Enhancing anode material performance represents a more effective and technically viable approach to boost LIBs performance compared to modifying other battery components. The theoretical specific capacity of commercial graphite anodes is 372 mAh g^{-1}, yet suffer from structural instability manifested as layer exfoliation during cycling, which compromises cycle stability and renders them inadequate for high-performance LIBs applications.[5-8] Promising inorganic anode candidates including alloy materials, conversion-type transition metal compounds, and silicon-based composites exhibit significant challenges such as substantial volume expansion and progressive capacity fade, ultimately undermining the cycling stability of LIBs systems.[9-12] This critical limitation necessitates the urgent development of novel high-performance anode materials capable of meeting evolving market requirements.[13]

Organic materials possess inherent advantages including environmental sustainability, structural tunability, and cost-effectiveness, garnering significant research attention.[14,15] The covalent bonding architecture of organic materials provides abundant redox-active sites that enable efficient interconversion between chemical and electrical energy via reversible electrochemical reactions. Despite their promise, organic materials face inherent limitations like electronic conductivity as well as poor solubility in organic electrolytes.[16-18] When directly employed as LIBs anodes, organic compounds exhibit suboptimal electrochemical performance due to these inherent material constraints. Two

Jiangxi Provincial Key Laboratory of Power Batteries & Energy Storage Materials, School of Materials Science and Engineering, Jiangxi University of Sciences and Technology, Ganzhou, 341000, China

**Email:* chenjun@jxust.edu.cn (Jun Chen)

[#]*These authors contributed equally to this work.*

primary approaches for improving the electro-chemical properties in organic materials were developed. The first approach involves fabricating organic-carbon composites, which effectively enhance electrical conductivity and cycling stability.[19,20] The second strategy focuses on engineering covalent organic frameworks (COFs) having precisely designed redox-active spots exhibiting high reversibility. COFs have garnered considerable attention a new category for porous organic materials, which are distinguished by their customisable pore structure and programmable framework structure.[21] The conjugated skeletons of COFs enable efficient charge carrier transport through π-π stacked electron cloud interactions and chemically adaptable channel environments, demonstrating exceptional promise for electrochemical energy storage applications.[22-24] The inherently porous architecture of COFs serves dual functions: mitigating dissolution of organic electrodes in electrolytes to enhance cycling stability, while simultaneously offering abundant redox-active sites for improved electrochemical performance.[25,26] Furthermore, the structural diversity of COFs encompassing varied topological configurations and connectivity modes establishes them as versatile platforms for precision engineering of organic functional materials.[27-29] However, the dynamic reversibility inherent in COF synthesis introduces polymerization degree variability that is critically dependent on reaction parameters. Therefore, on the basis of the complex structure of the feedstock monomers with a high number of functional groups, conducting multidirectional and complex organic polymerization reactions will lead to the still great challenge of how to pre-design and efficiently control the structure of COFs as well as the degree of polymerization.[30-33] TPPDA (tetrakis(4-aminophenyl)phenylenediamine), due to its tetraamino symmetric structure and rigid conjugated backbone, can be used as a multifunctional cross-linking agent to form stable covalent organic frameworks (COFs) with the nitro group of nickel phthalocyanine (NiPc) via an azo coupling reaction. Among them, the highly reactive amino group (-NH_2) of TPPDA can efficiently anchor NiPc-$(NO_2)_4$, while nickel phthalocyanine (NiPc) is a class of conjugated compounds with 18 π-electrons, numerous C=N unsaturated functional groups, and a benzene-ring conjugated structure, which can provide an effective embedding/de-embedding Li^+ channels.[34-36] Copolymerizing Pc monomers enables dual advantages: harnessing intrinsic unsaturated functionalities while constructing COF networks with enhanced redox-active site density, thereby significantly boosting the electrochemical properties of polymeric systems. This methodology establishes a promising avenue for advancing next-generation organic anode materials in LIB technologies.[37-39]

Herein, this work illustrates a controlled synthesis for phthalocyanine-based covalent organic frameworks (Pc-COFs), designated as TPPDA-NiPc, to establish structure-property relationships between monomer stoichiometry, polymerization degree, and electrochemical energy storage characteristics. Through precise stoichiometric control of tetrakis(4-aminophenyl) phenylenediamine (TPPDA) to nickel phthalocyanine (NiPc) at molar ratios of 2:1, 1:1, and 1:2, the derived Pc-COFs displayed tunable polymerization degrees and optimized density of redox-active sites within their extended network architectures. Ultimately, the electrochemical properties of TPPDA-NiPc materials were effectively improved. This systematic investigation reveals that elevating phthalocyanine content modulates supramolecular polymerization kinetics, offering fundamental guidelines for designing high-capacity organic electrodes through rational monomer engineering in Pc-COF systems.

2. Experiments

2.1 Materials

4-Nitrophthalonitrile, n-pentanol, cobalt chloride hexahydrate, DBU, sodium sulfide hydrate, N'N'-tetraaminophenyl-p-phenylenediamine (TPPDA), DMF, acetone, tetrahydrofuran, anhydrous ethanol, N-methylpyrrolidone (NMP), polyvinylidene fluoride (PVDF), and conductive carbon black (SP) were all were purchased from Chemical Reagent Co. without any purification before use.

2.2 Synthesis

2.2.1 Synthesis of tetranitronickel phthalocyanine

First, 4-nitrophthalonitrile (17.30 g, 0.1 mol) and n-pentanol (250 mL) were placed in a three-necked flask and stirred magnetically for 2 h to remove oxygen; then the temperature was raised to 60 °C and held for 35 min and 7-8 drops of DBU were added to the solution; when the temperature was raised to the point that the solution became discoloured, 3.37 g of anhydrous nickel chloride was added. The air in the reaction system was replaced by a three-pump, three-charge method. The nitrogen flow rate (50 mL min^{-1}) and nitrogen purity were 99.99%. The whole polymerisation process (from the start of the reaction to cooling) was carried out under nitrogen protection at a temperature of 135 degree Celsius for 65 hours. At the end of the reaction, anhydrous ethanol was added for several times to wash, decontaminate and filter, and the filtrate was clarified, and the solid product was dried in a vacuum drying oven at 60 °C for one day to obtain nickel tetranitrophthalocyanine (NiPc-$(NO_2)_4$).

2.2.2 Synthesis of TPPDA-NiPc (2:1)/(1:1)/(1:2)

A mixture of TPPDA (1.2287 g, 2.6 mmol), tetranitrophthalocyanine nickel(II) (0.9818 g, 1.3 mmol), KOH (0.72 g, 12.8 mmol) was sequentially charged with 150 mL of DMF in a three-neck flask. Mixture is sonicated for 30 minutes and then warmed up with stirring at 150 °C over 24 hours. When the reaction was complete, an appropriate quantity of distilled water was poured into the cooled mixture which was left to filter. Products were washed thoroughly byTHF, acetone and anhydrous ethanol. Lastly, it was dried at 60 °C over 24 hours to yield TPPDA-NiPc (2:1).Similarly, TPPDA-NiPc (1:1) and TPPDA-NiPc (1:2) were prepared by adjusting the molar ratios of TPPDA (1.95 mmol, 1.3 mmol)

to nickel(II) tetranitrophthalocyanine (1.95 mmol, 2.6 mmol), respectively, while maintaining the same amount of KOH (12.8 mmol) and following the identical synthetic procedure.

2.3 Battery assembly and performance testing

2.3.1 Battery assembly

The slurry was prepared by mixing the active material TPPDA-NiPc, conductive agent SP, and binder PVDF in N-methyl-2-pyrrolidone (NMP) at a mass ratio of 6:3:1. Specifically, PVDF was first completely dissolved in NMP at 120 °C, followed by sequential addition of the active material and conductive carbon black in the prescribed ratio. The mixture was then sealed and ball-milled at 18 H_z for 12 hours. The resulting slurry was uniformly coated onto copper foil current collectors, followed by drying, calendering, and punching into 14 mm diameter circular anode electrodes, with each electrode weighing 12.2 mg and having an areal density of 0.54 mg cm^{-2}. Cell assembly was performed in an argon-filled glove box using: a 0.6 mm thick lithium wafers as the counter electrode, 1M $LiPF_6$ in DEC/EMC/EC (1:1:1 by volume) as the electrolyte, and Celdard 2400 separators. The coin-type half-cells were assembled in the following sequence: negative shell → lithium wafers→ separator → electrolyte → COFs electrode → spacer → spring sheet → positive shell. A pressure of 600 MPa was maintained for 5 seconds, and electrochemical testing commenced after 12 hours of complete electrolyte wetting.

2.3.2 Material structure characterization

The structure was characterised using a Bruker IFS66/S FTIR spectrometer in the range of 400-4000 cm^{-1}. The functional group vibration information of the sample was obtained by KBr tablet method. Crystal structural analyses were carried out with a Bruker D8 Advance X-ray diffractometer equipped with a Cu Kα radiation source (λ = 0.15406 nm), scanning angles ranging from 1 to 90 °, and pore sizes for COFs materials were analysed. Specific surface area and pore size distribution were tested by Specific Surface Area Analyser Model 3H-2000PS2. After the samples were pretreated by vacuum drying and dehydrated at 120 °C for 2 hours, the isotherms of N2 adsorption and desorption were measured at 77 K liquid nitrogen temperature to analyse specific area and pore size distribution of organic framework materials. The micro-morphology and particle size of the materials were visualised with a ZEISS Crossbeam 340 Field Emission Scanning Electron Microscope (accelerating voltage 5 kV) and surface scans were carried out with an Oxford X-Max 80 Energy Spectrometer to analyse the distribution of the various elements. The microstructure and stacking of organic frame materials were analyzed by JEOL JEM2100F mode field emission transmission electron microscope (accelerated voltage 200 kV). The surface chemical state was analyzed by Thermo Scientific K-Alpha X-ray photoelectron spectrometer with Al Kα as the excitation source to investigate the valence state transition rule of electrode materials under different charging and discharging states.

2.3.3 Electrochemical performance test

In this study, a LAND CT2001A battery test system was used to perform constant-current charge/discharge tests on button cell batteries, in which the operating voltage window was set to 0.01-3.0 V. Increasing current densities (0.05, 0.1, 0.2, 0.5, 1.0, and 2.0 A g^{-1}) were set to evaluate the multiplicity performance of the batteries. Cyclic voltammetry (CV) testing is completed at voltages ranging from 0.01-3.0 V using the IviumStat.XR electrochemical workstation. CV tests were performed with the IviumStat XR electrochemical workstation. The base scan rate was set at 0.1 mV s^{-1}, and the redox properties were also systematically investigated in this thesis at five gradient scan rates in the 0.1-0.5 mV s^{-1} interval. Electrochemical impedance (EIS) tests were performed with a Swiss Aptar electrochemical workstation, NOVA 2.1 with a frequency range of 0.01-200 H_z and a voltage magnitude from 10 mV.

3. Results and discussion

3.1 Material characterization

The synthesis protocol commenced with preparation of tetranitro nickel phthalocyanine (TN-NiPc) via nucleophilic substitution between 4-nitrophthalonitrile and $NiCl_2$. A series of azo-linked TPPDA-NiPc COFs with controlled stoichiometric ratios (2:1, 1:1, 1:2) were synthesized through thermally activated (150 °C) azo-condensation of TPPDA and TN-NiPc precursors (Fig. 1a). This azo-condensation approach was strategically selected for constructing conjugated polymers due to its catalyst-free operation, synthetic efficiency, and structural precision. Furthermore, the incorporated azo linkages establish electron-dense conjugated networks that facilitate charge carrier mobility and enhance electrochemical redox kinetics. X-ray diffraction (XRD) patterns (Fig. 1b) showed that the monomer ratio mainly affected the degree of polymerisation and local bonding mode, but the basic topology (e.g., AA stacking) was determined by the geometrical conformation of the monomers. Thus, all three COF materials showed a characteristic diffraction peak at 6.01°, corresponding to a polymer network framework size of 1.47 nm, and a peak at 26.78°, corresponding to an interlayer spacing of 3.33 Å. It is noteworthy that the diffraction peak positions of the three COFs are highly consistent, with little difference in their framework dimensions and almost no difference in the interlayer voids. This result suggests that the reaction system tends to form TPPDA-NiPc with the same topology despite the change in the monomer ratio. In addition, the measured frame sizes of the XRD plots of the three COFs are in good agreement with the theoretical optimization model. In addition, structural optimization showed (Fig. 1c) that TPPDA-NiPc has an AA-type stacked square biporous structure with micropores of about 1.5 nm in size and 0.33 nm

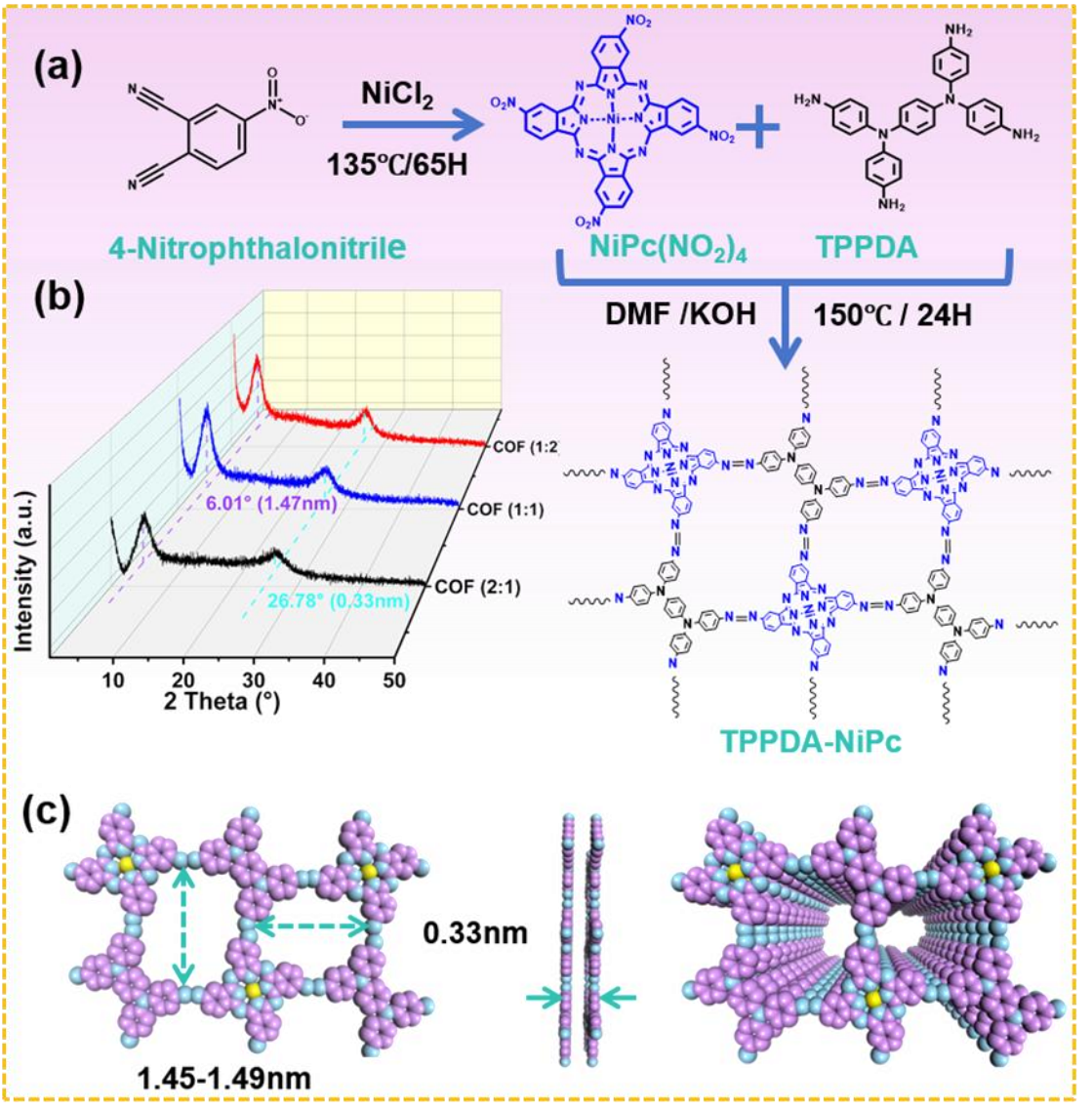

Fig. 1: TPPDA-NiPc (2:1)/(1:1)/(1:2): (a) Synthesis schematic; (b) XRD pattern; (c) Optimization of framework structure.

layer spacing in its backbone, and these structural features provide effective transport channels for the embedding/denegration of Li^+. The polymer exhibits insoluble properties in the electrolyte providing excellent electrochemical performance. However, the polymerization reactions of COFs synthesized from different monomer ratios are somewhat reversible, and the degree of polymerization of the polymers is affected by the reaction conditions, leading to differences in the electrochemical properties of the materials. In an endeavor to systematically explore the impact of monomer ratio on the synthesis of COFs, a comprehensive characterization was carried out using Fourier Transform Infrared Spectroscopy (FTIR), Raman Spectroscopy, and Nitrogen Adsorption-Desorption Testing (BET). The obtained results were found to be congruent with the theoretical anticipations. Specifically, the FTIR spectra indicated that the peaks positioned at 757 cm^{-1}, 1096 cm^{-1}, and 1136 cm^{-1} could be ascribed by conjugated structure in phthalocyanine as well as the bending vibration in C-H bond (Fig. 2a). Moreover, peaks at 1334 cm^{-1}, 1616 cm^{-1} and 1726 cm^{-1} were observed corresponding with characteristic absorption peaks of nitro (-NO_2) on the phthalocyanine ring, along with C=N as well as C=C bonds within a phthalocyanine ring. Thereby effectively validating the successful synthesis of nitro phthalocyanine. Notably, the characteristic peaks of a pair of amino groups, which were located in the range of 3300 - 3500 cm^{-1}, could be distinctly observed in TPPDA. In (Fig. 2b), all of the TPPDA-NiPc COFs synthesised in three different ratios (2:1, 1:1, 1:2) maintained the characteristic C=N-bond peak located to 1616 cm^{-1} of the phthalocyanine ring; in contrast, an original nitro characteristic peak (located to 1726 cm^{-1}) essentially disappeared. (Fig. 2c) presents a clear zoomed-in regional infrared spectrum in which an amino character peak located in the range of 3300 - 3500 cm^{-1} is still clearly discernible.[40] This result implies that the prepared polymer underwent an incomplete reaction, with a small quantity of unreacted amino functional groups persisting within the structural network. Nonetheless, the residual amino signals of TPPDA-NiPc (2:1) were markedly stronger in comparison to those of the other two groups of COFs, and exhibited a downward tendency as

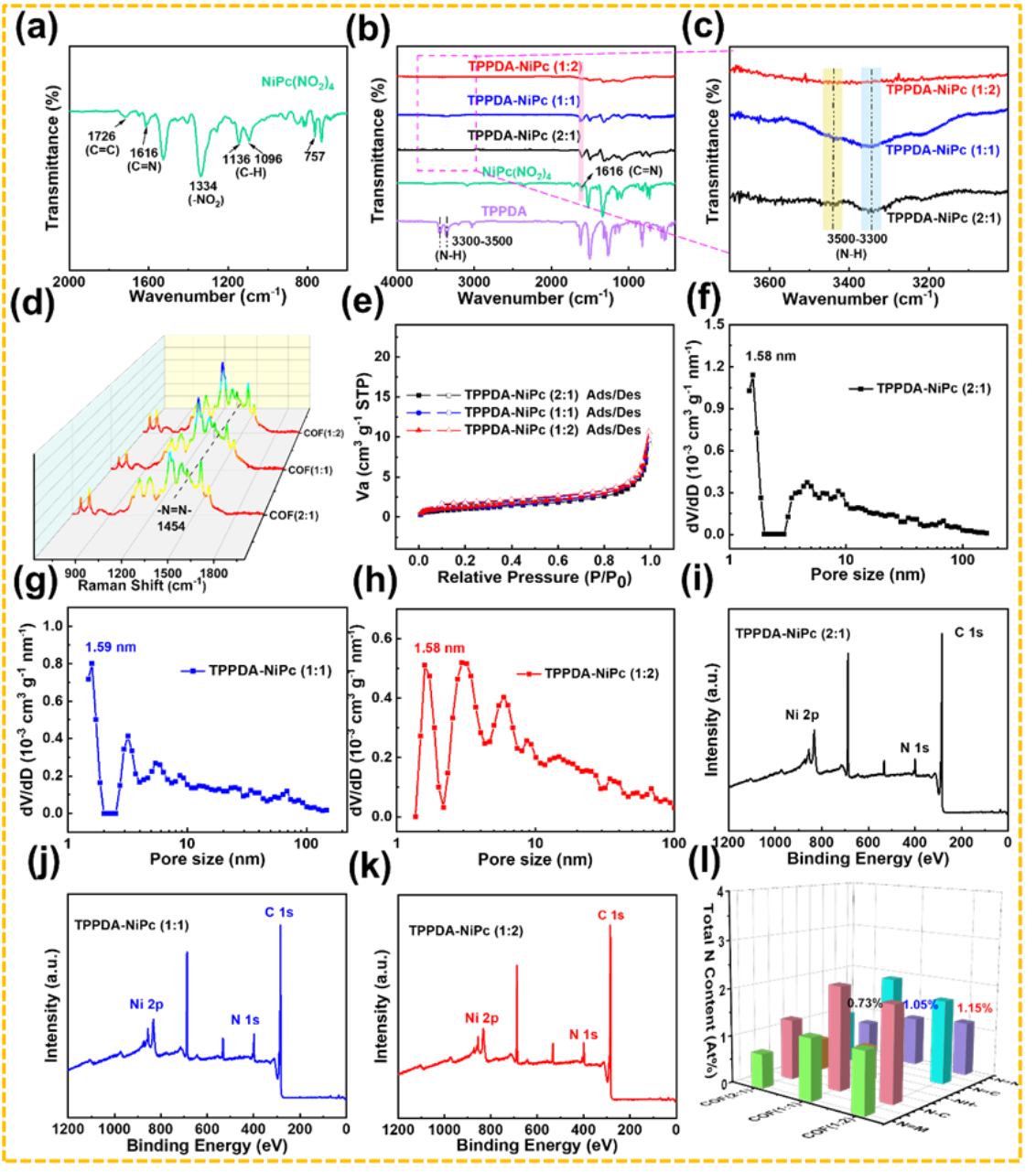

Fig. 2: FTIR spectra of NiPc(NO_2) (a); FTIR spectra of TPPDA-NiPc (2:1)/(1:1)/(1:2) (b,c); Raman spectra (d); nitrogen adsorption-desorption isotherms (e); corresponding pore size distributions (f,g,h); XPS full spectra (i,j,k); maps of nitrogen content of each component (l).

the proportion of phthalocyanine monomer augmented. Among them, the characteristic peaks corresponding to residual amines were scarcely detectable in TPPDA-NiPc (1:2). This observation effectively demonstrates distinct differences in the network structures of the COFs synthesized from the three monomer ratios, indicating varying degrees of organic polymerization. Notably, the polymerization degree appears to increase with a higher proportion of phthalocyanine units. The detection of N=N groups by IR spectroscopy was limited with presence on C=N, so further Raman spectroscopy was performed for these three COFs. A characteristic peak at 1454 cm^{-1} of -N=N- was clearly observed (Fig. 2d), confirming successful azo bond formation. Furthermore, the intensity of azo group characteristic peaks in the COFs' Raman spectra progressively increased with higher phthalocyanine monomer content, indicating that TPPDA-NiPc (1:2) possessed a more complete network structure and higher polymerization degree. In an attempt to systematically characterize the pore structure distribution of the TPPDA-NiPc materials, the nitrogen adsorption-desorption isotherms at 77 K as well as the corresponding specific surface areas of the three materials were tested in this study (Fig. 2e). The results demonstrate that all three COFs exhibit low specific surface areas, primarily due to the tight π-π stacking among the molecular levels. However, the micropores (1.5 nm) and layer spacing (0.33 nm) provide Li^+ transport channels, and the surface pseudocapacitance contribution compensates for diffusion limitations, and does not limit Li+transport

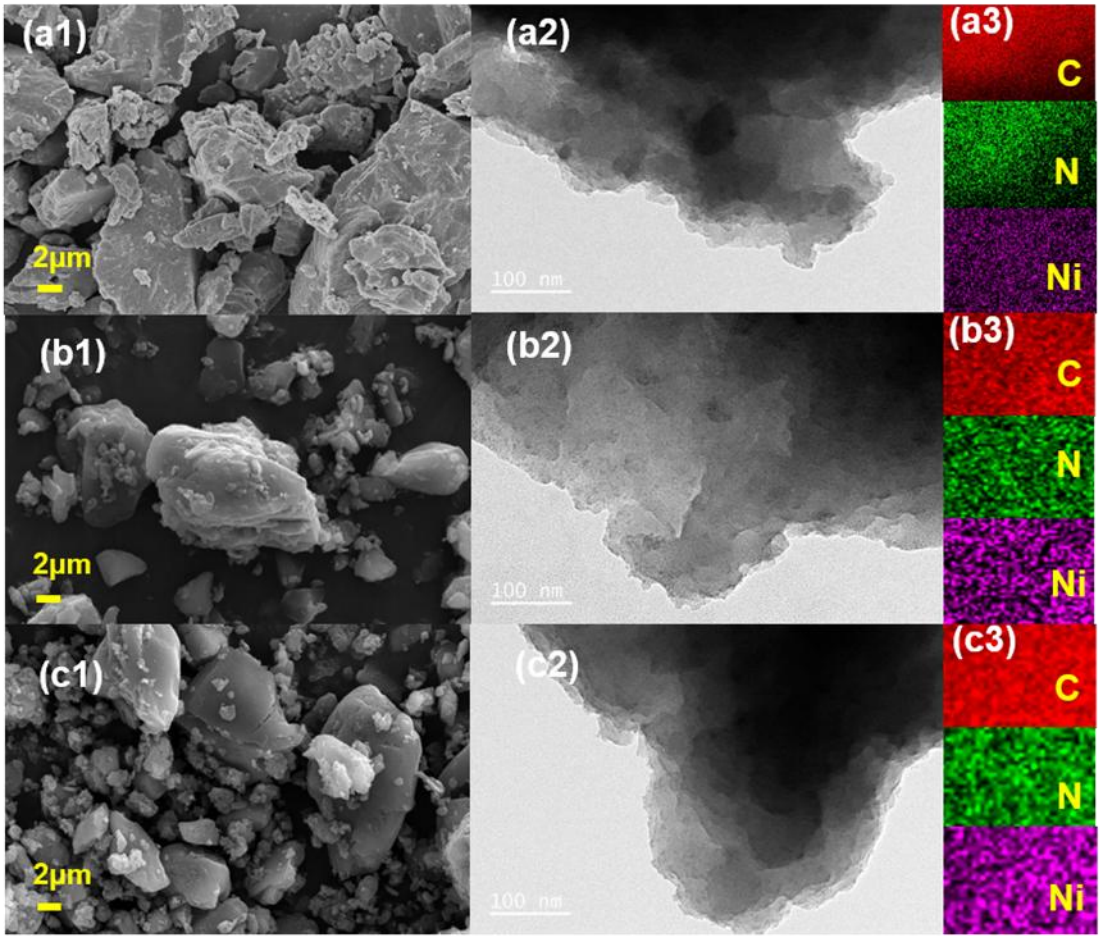

Fig. 3: SEM and EDS images of TPPDA-NiPc (2:1)/(1:1)/(1:2): (a) TPPDA-NiPc (2:1); (b) TPPDA-NiPc (1:1); (c) TPPDA-NiPc (1:2).

Furthermore, the pore size distribution curves of TPPDA-NiPc materials (Fig. 2f-h) reveal that the predominant pore sizes for all three COFs range from 1.58 to 1.59 nm. This suggests that the two monomers maintain consistent bonding connectivity despite varying monomer ratios, which is corroborated by the XRD patterns. Additionally, the synthesized TPPDA-NiPc materials with three monomer ratios exhibit several distinct peaks, arising from structural interpenetration during polymerization that generates mesoporous and macroporous structures, as evidenced by the adsorption-desorption isotherm. To thoroughly analyze the chemical composition, the three TPPDA-NiPc COFs were examined by X-ray photoelectron spectroscopy (XPS). The XPS surveying spectrum for all three COFs displayed characteristic peaks for C 1s, N 1s, and Ni 2p (Fig. 2i-k), confirming the phthalocyanine incorporation and demonstrating successful polymerization. Combined with the fine spectra of N 1s (Fig. S4), the contents of the groups corresponding to various N elements were represented by (Fig. 2l), including the five nitrogen-containing fractions of N-M (M stands for metal ions), N=C, -NH2, N-C, and N=N. The N=N group contents measured 0.73%, 1.05%, and 1.15% for the three COFs, showing a positive correlation with phthalocyanine monomer content that peaked at the TPPDA:NiPc (1:2) ratio.

The microscopic morphology of the three COFs was characterized by scanning electron microscopy (SEM). SEM images revealed that TPPDA-NiPc comprised agglomerated particles with varying sizes and irregular shapes (Fig. 3a1-c1). The particles exhibited a broad size distribution (1-8 μm) with an average diameter of ~4 μm, displaying a layered, lumpy morphology (Fig. S1 a1-c1). This morphology is consistent with the microscopic characteristics of azo-phthalocyanine-based COFs reported in previous studies.[38] Notably, increasing the phthalocyanine content leads to the appearance of more small particles with mild aggregation in the COFs. Furthermore, EDS mapping (Fig. 3a3-c3) revealed homogeneous distributions for C, N with Ni elements within TPPDA-NiPc samples without significant agglomeration, demonstrating excellent compositional uniformity. To investigate the microstructure and crystallinity of TPPDA-NiPc in greater detail, transmission electron microscopy (TEM) was performed. TEM (Fig. 3a2-c2) demonstrate that all three COF samples exhibit pronounced aggregation with dispersed, non-uniform layered structures. However, high-resolution TEM images (Fig. S1 a2-c2) did not reveal distinct lattice fringes, a characteristic attributable from the unique structural as well as chemical properties for COF materials. These observations is consistent with the low crystallinity shown by XRD analysis, so it is difficult to observe distinct lattice stripe.

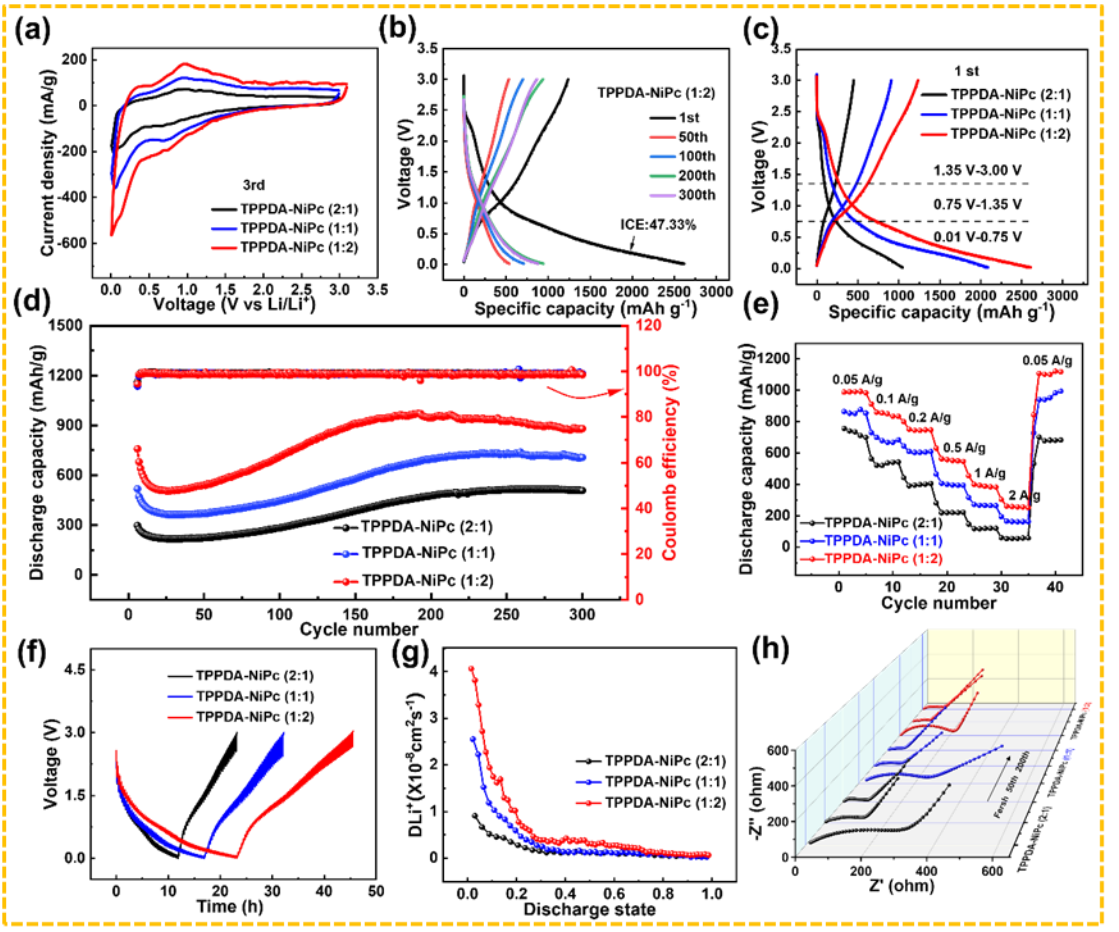

Fig. 4: (a) Third turn CV curves of TPPDA-NiPc (2:1)/(1:1)/(1:2). (b) Charge-discharge curve of TPPDA-NiPc (1:2) at 100 mA g^{-1} current density. (c) First-turn charge/discharge curves for the three COFs electrodes. Electrochemical testing of TPPDA-NiPc (2:1)/(1:1)/(1:2) (d) Long cycling at 100 mA g^{-1} current density; (e) Rate capability; (f,g) GITT and (h) electrochemical impedance mapping.

As demonstrated by the structural characterization tests of the COFs materials described above, there are differences in the network structure of the COFs synthesized with three different monomer ratios. The degree of organic polymerization varies, exhibiting a progressive increase as the phthalocyanine monomer ratio rises. To evaluate this electrochemical property for COF-based electrodes, three COF samples were assembled into a CR2032 coin cell (lithium metal was used as the counter electrode).

A series of electrochemical tests were systematically performed, including cyclic voltammetry (CV), galvanostatic charge-discharge (GCD), rate capability measurements, and electrochemical impedance spectroscopy (EIS). The CV profiles of the three COFs (Fig. S2a-c) exhibit relatively weak redox peaks, which is attributed to the nature of COFs polymers that are prone to interlayer stacking and have a porous architecture. This structural feature results in the COFs materials being prone to polarization in the redox reaction with Li^+, which in turn triggers a change in the voltage plateau. The first-lap CV profiles of TPPDA-NiPc (2:1) exhibit three distinct redox peak pairs at 2.60/2.23 V, 0.96/0.88 V, and 0.33/0.06 V, while TPPDA-NiPc (1:1) and (1:2) display redox features at comparable potentials. Based on the chemical structure of TPPDA-NiPc COF, The redox couple at 2.60/2.23 V is attributed to a reversible redox process with C=N as well as N=N functional groups coordinated by Li^+. Meanwhile, the redox peak located at 0.96 V/0.88 V is formed by the macrocyclic conjugated structure of the phthalocyanine unit in the COFs and the lithiation reaction of the unsaturated C=C in the benzene ring.[41,42] In additional, a redox peak of 0.33 V/0.06 V reflects the electrochemical reaction of the network-structured channels of the COFs compounds and the interlayer voids with Li^+. The markedly reduced integrated area of post-first-lap CV scans, which clearly indicates that a solid electrolyte interphase (SEI) layer is formed during the initial lithiation process, accounting for the observed irreversible capacity. Notably, the near-perfect overlap between second and third-lap CV profiles demonstrates outstanding electrochemical reversibility and confirms the material's excellent cycling stability. The COFs synthesized with three distinct monomer ratios exhibit variations in their network architectures, leading to differing degrees of organic polymerization and consequently, divergent electrochemical performance in their respective electrodes. As depicted in

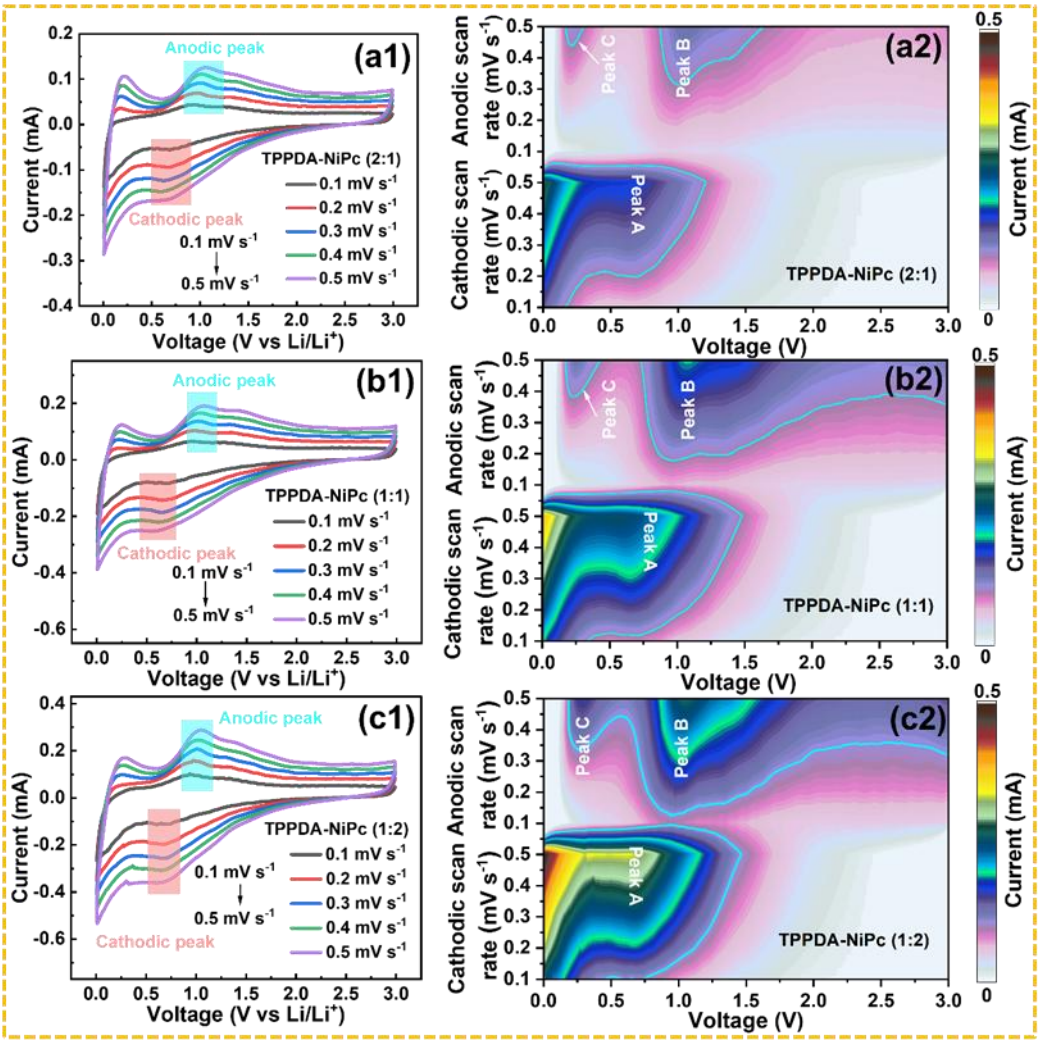

Fig. 5: CVs and peak currents (a1,b1,c1) of TPPDA-NiPc (2:1)/(1:1)/(1:2) at different scan rates; CV cloud plots (a2, b2, c2).

(Fig 4a), the areas for a CV closure curve in the third ring for TPPDA-NiPc (2:1)/(1:1)/(1:2) electrodes exhibit an increasing trend, which effectively indicates that the network structure of TPPDA-NiPc (1:2) is more complete, with a higher degree of organic polymerization reaction and more redox-active sites, thereby facilitating improved electrochemical capacity.

To assess the lithiation/delithiation reversibility of TPPDA-NiPc, electrostatic charging/discharging experiments have been performed from 0.01 to 3.0 V. (Fig. 4b, S3a,b). The initial discharge capacities of the TPPDA-NiPc (2:1), (1:1), and (1:2) electrodes were 1049, 2094, as well as 2617 mAh g^{-1}, respectively. Corresponding initial Coulombic efficiencies of 43.23%, 43.61%, and 47.33% align with the typically low first-cycle efficiency observed for organic electrode materials. The substantial irreversible capacity in organic electrode materials mainly originates from three contributing factors. First, some of the active Li^+ are consumed by the SEI membrane. Second, the electrolyte undergoes an irreversible decomposition reaction on the electrode surface. Thirdly, structural changes in the electrode material during deep discharge can lead to irreversible Li^+ de-embedding.

It is noteworthy that as the proportion of phthalocyanine units increases, the network structure of TPPDA-NiPc becomes more complete. This leads to a more pronounced degree of organic polymerization, a higher content of corresponding N=N functional groups, and an increased number of available redox-active sites. Collectively, these features facilitate electrochemical processes, leading to improved capacity Analysis of the first lap charge/discharge curves for three COFs revealed the presence of three distinct voltage plateaus (0.01-0.75 V, 0.75-1.35 V and 1.35-3.0 V), which exhibited a high degree of concordance with the redox peaks observed through CV analysis (Fig. 4c). However, the charge/discharge curves corresponding to the subsequent cycles did not exhibit a discernible voltage plateau. This phenomenon was attributed a polarisation in the porous material by electrochemical redox procedures.

Cycling stability for LIBs serves as a crucial metric for evaluating practical applicability, providing insights into electrode structural integrity, side reaction extent, charge transfer efficiency, and reaction kinetics. In this work, the cycling performance of three electrodes with different COF ratios was tested at a current density of 100 mA g^{-1} . (Fig. 4d) Upon reaching the 25th cycle, the TPPDA-NiPc (2:1), (1:1), and (1:2) electrodes attained minimum discharge capacities of

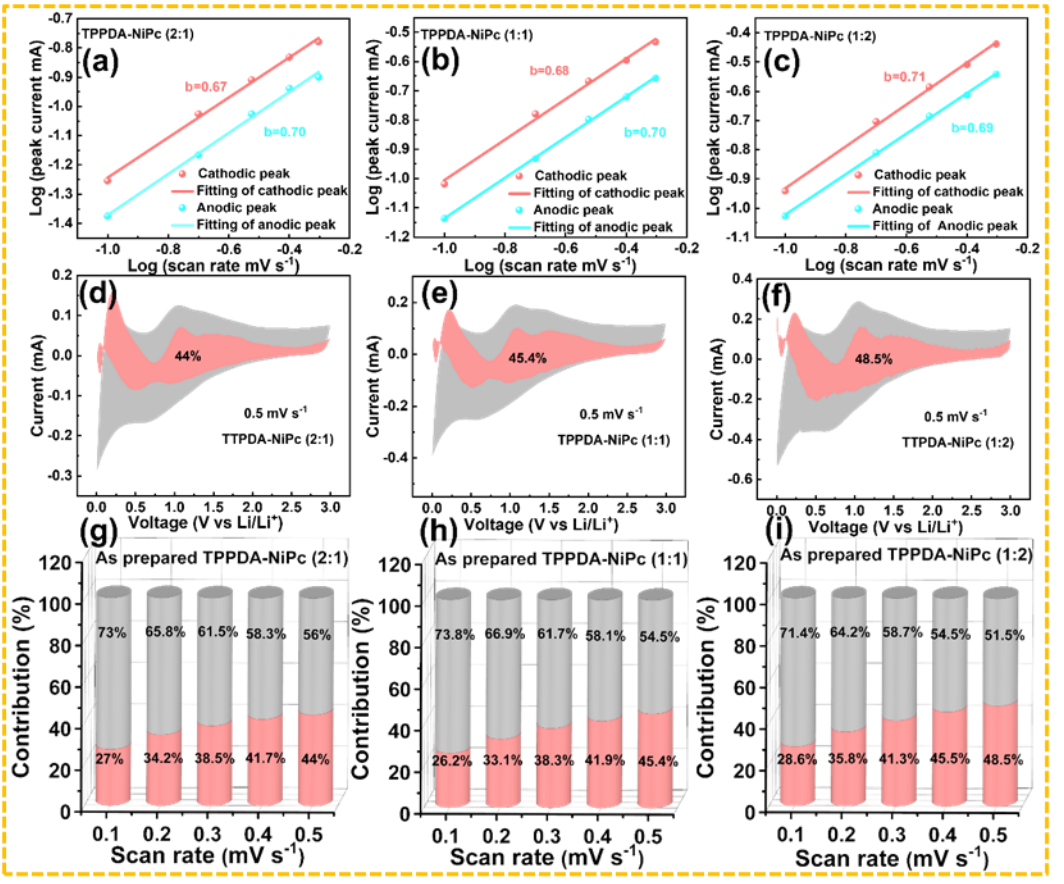

Fig. 6: Linear relationship between TPPDA-NiPc (2:1)/(1:1)/(1:2) spike current and scan rate square root (a, b, c); CV curves and pseudocapacitance percentage plots with 0.5 mV s^{-1} (d, e, f); pseudocapacitance percentage contribution at different scan rates (g, h, i).

216.7, 361.7, and 502.6 mAh g^{-1}, respectively, followed by gradual capacity recovery. The initial capacity decay observed in all three COF electrodes primarily originated from SEI layer formation on the electrode-electrolyte interface, leading to active site consumption and irreversible capacity loss.[43,44] The TPPDA-NiPc (2:1), (1:1), and (1:2) electrodes achieved maximum specific capacities of 516.9, 732.1, and 970.5 mAh g^{-1} during cycles 200-250, followed by a stable period with minimal capacity decay. After 300 cycles, the three materials still maintained the increment of 290.9, 344.9 and 377 mAh g^{-1} at the lowest specific capacity. Compared with commercial graphite anodes (theoretical capacity 372 mAh g^{-1}, actual capacity ~350 mAh g^{-1}), the TPPDA-NiPc (1:2) electrode exhibits a reversible capacity of 970.5 mAh g^{-1}at 100 mA g^{-1}, which is 2.7 times that of graphite. This performance advantage stems from the abundant redox active sites and stable covalent network structure in the phthalocyanine framework, indicating its potential to replace traditional carbon-based anodes in the next-generation high-energy-density batteries. Notably, phthalocyanine-based COFs possess both a stable porous network facilitating Li^+ transport and a π-π conjugated system enabling efficient charge transfer within phthalocyanine units. This dual functionality creates synergistic effects that substantially improve overall material performance. Furthermore, higher phthalocyanine content enhances polymerization degree and N=N group density in TPPDA-NiPc (1:2), boost electrochemical activity.

Rate capability serves as a critical metric for assessing electrode kinetics and capacity retention under varying current densities. The rate capability of three COF electrodes was evaluated via a step-current protocol. (Fig. 4e) When the current density is 0.05, 0.1, 0.2, 0.5, 1 and 2 A g^{-1}, TPPDA-NiPc (2:1) delivered capacities of 735.4, 536.4, 398.8, 219.1, 119.8, and 56.9 mAh g^{-1}, while TPPDA-NiPc (1:1) exhibited 852.8, 667.9, 603.4, 400, 264.8, and 162.2 mAh g^{-1}. Under identical conditions, TPPDA-NiPc (1:2) demonstrated superior rate performance with discharge capacities of 992.1, 850.0, 744.4, 557.9, 384.4, and 255.5 mAh g^{-1}. Upon high current discharge, the capacities of TPPDA-NiPc (2:1), TPPDA-NiPc (1:1), and TPPDA-NiPc (1:2) still recovered to 680.6, 983.6, and 1121.7 mAh g^{-1}, respectively, when current density was decreased to 0.05 A g^{-1}, respectively. Restricted ion transport within the porous polymer network primarily accounts for the capacity fading at elevated current densities. Collectively, these results demonstrate that that the TPPDA-NiPc (1:2) material exhibits more remarkable electrochemical performance compared to the other two materials with different ratios of COFs. This effectively proves that the TPPDA-NiPc (1:2) material exposes more effective active sites, which is favorable for charge storage. It has faster ion

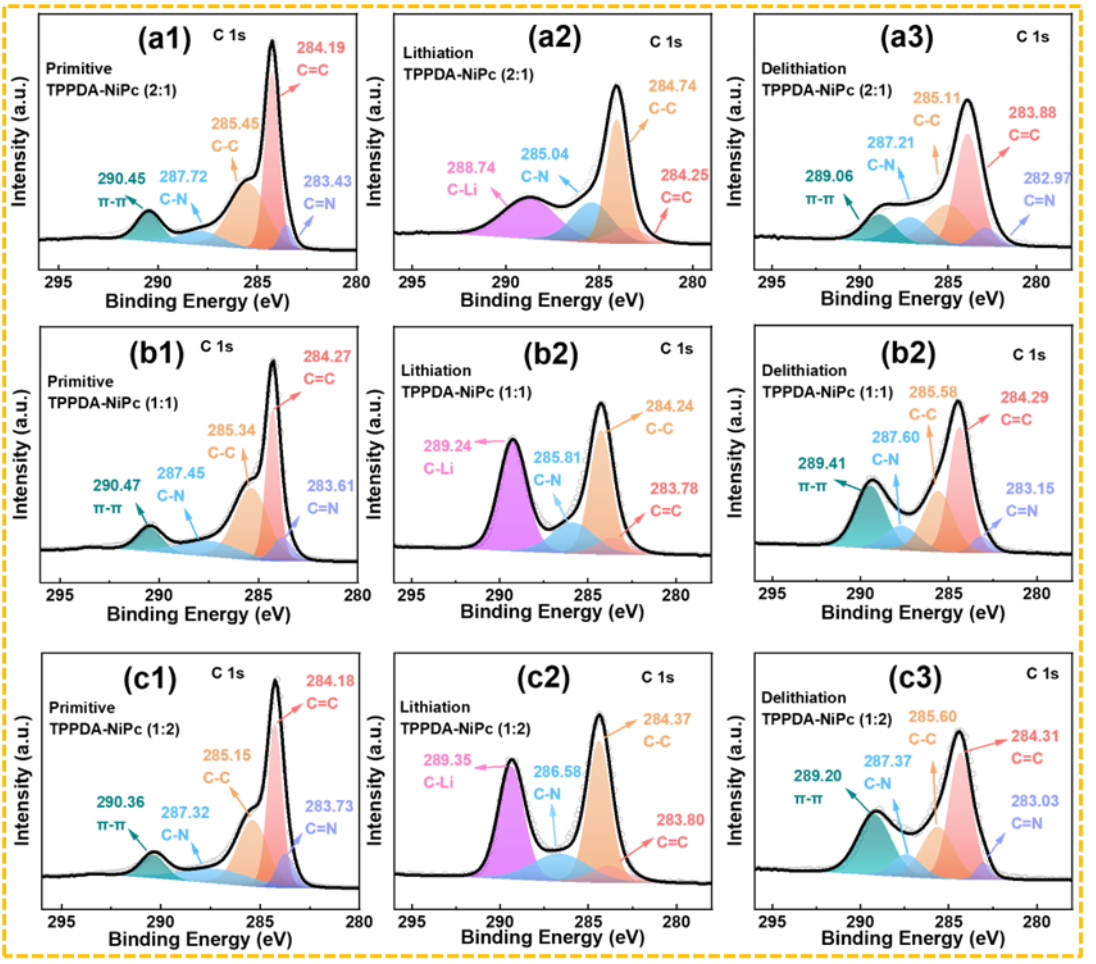

Fig. 7: XPS C 1s profiles of TPPDA-NiPc (2:1)/(1:1)/(1:2) electrode materials under pristine (a1, b1, c1) and discharged (a2, b2, c2) and charged (a3, b3, c3) conditions.

migration rate and promotes charge transport kinetics.

To elucidate the intrinsic electrochemical lithium storage mechanism of TPPDA-NiPc materials, Three COF electrodes were systematically characterised through electrochemical impedance spectroscopy (EIS) as well as constant current intermittent titration technique (GITT). An equivalent circuit model from (Fig. S6) was used for fitting, while (Table S7) aggregates its corresponding fitted figures. Here, Rf denotes resistance to Li^+ diffusion and migration across this SEI membrane (i.e., interfacial resistance), Rct denotes charge transference resistance within electrochemical reaction processes, W1 corresponds to the Warburg resistance, which reflects the Li^+ diffusion resistance within the electrode material. The initial Rct values of the as-prepared TPPDA-NiPc (2:1), (1:1), and (1:2) electrodes measured 336.8 Ω, 232.6 Ω, and 188.6 Ω, respectively. (Fig. 4h) After 50 cycles, the Rct values of TPPDA-NiPc (2:1) and (1:1) decreased to 116.5 Ω and 48.5 Ω, respectively, with further reduction to 71.49 Ω and 35.9 Ω after 200 cycles. In contrast, TPPDA-NiPc (1:2) exhibited superior stability, demonstrating Rct values of merely 38.6 Ω after 50 cycles and 35.4 Ω after 200 cycles. EIS analysis revealed that the electrode displayed elevated Rct prior to initial cycling, stemming from two primary factors: (1) Blockage of the porous network voids within the COF electrode materials, restricting ion transport pathways; (2) Inadequate wetting contact at the electrode-electrolyte interface. This interfacial contact impedance substantially influences the initial electrochemical performance. The cycling activation process facilitated gradual pore-structure expansion in the COFs, enhancing Li^+ mobility and thereby reducing Rct values. These results suggest that the electrodes underwent gradual activation during cycling, resulting in superior Li^+ transport kinetics. To further investigate the reaction kinetics, TPPDA-NiPc was characterized by GITT. From, (Fig. 4f,g) It is seen that TPPDA-NiPc (1:2) electrode has a higher lithium diffusion coefficient than the other two ratios of COFs electrodes, which further validates the previous conclusion.

To investigate the lithium storage mechanism in the three COFs, we performed electrochemical characterization via cyclic voltammetry at five scan rates. (Fig. 5a1-c1) From the current-potential responses at various scan rates, we constructed redox peak cloud diagrams. (Fig. 5a2-c2) Where peaks A and B represent the redox peaks corresponding to the reversible electrochemical reaction between the macrocyclic conjugated structure of phthalocyanine and C=C groups from benzene ring and Li^+ in TPPDA-NiPc compounds, and the oxidation peaks represented by Peak C reflect the

electrochemical reaction between the network-structured channels of the COFs and the voids in the interlayers and the Li^+. The oxidation peak (Peak B) of TPPDA-NiPc (2:1) displays a narrower current response range, (Fig. 5a2) suggesting a lower reaction rate. This implies that the macrocyclic conjugated structure of phthalocyanine units and C=C functional groups in benzene rings exhibit weaker Li^+ binding at higher scan rates. Correspondingly, the electrode demonstrates a constrained electrochemical response at Peak C. In contrast, the oxidation peaks corresponding to the cloud diagrams of the TPPDA-NiPc (1:1) and (1:2) electrodes exhibited a wider range of current response, (Fig. 5b2, c2) indicating superior redox activity. As the proportion of phthalocyanine units and the extent of the organic polymerization reaction increase, the TPPDA-NiPc(1:2) material provides a more efficient redox active site, which binds more tightly to Li^+, and the change in current response with scan rate is more pronounced in the CV cloud.

Previous studies indicate that when active material particles in energy storage electrodes approach nanoscale dimensions, Linear correlation of peak current with square root scan rate can be established according to Eq. (1)[45], which allows us to demonstrate whether the total electrochemical kinetic response of the electrode material is a diffusion-controlled intercalation process (battery behavior) or a surface-controlled pseudocapacitance process (pseudocapacitance behavior).

$$i(V) = av^b \quad (1)$$

Here, i denotes peak current (A), v represents the sweep rate (mV s^{-1}), the slope b can be calculated from the above equation. If lithium storage mechanism in electrode materials becomes diffusion-controlled, b = 0.5; theoretical b > 1 if the electrochemical kinetic response is surface-controlled; while b is in the range of 0.5-1, it indicates that both control mechanisms are functioning. In (Fig. 6a-c) a b-value of 0.67/0.70, 0.68/0.70 as well as 0.71/0.69 on oxidation-reduction peaks of the three COF pristine electrodes, sufficiently indicating the lithium storage mechanism for the three electrode materials is controlled in both diffusion and surface-controlled ways.

At the maximum scan rate (0.5 mV s^{-1}), pseudo-capacitance contributions from three COF electrodes reached 44.0%, 45.4%, and 48.5%, respectively. (Fig. 6d-f) The ratios of the pseudocapacitance contributions of the three COFs electrode materials were systematically investigated at different rates within a range from 0.1-0.5 mV s^{-1}. Data analysis (Fig. 6g-i) revealed that the pseudocapacitance contribution rose markedly with increasing scan rate: from 27.0% to 44.0% for TPPDA-NiPc (2:1), from 26.2% to 45.4% for (1:1), and from 28.6% to 48.5% for (1:2). As the scan rate increases, there is an increasing contribution to pseudocapacitance from the three COFs electrodes, which indicates a significant shift in electrochemical kinetic behaviour in electrode materials (a gradual shift from diffusion-controlled to surface-controlled predominance), which effectively proves a significant increase in the diffusion rate of Li^+. Furthermore, during successive cycles, with the continuous activation in the active material, LIBs capacity is gradually enhanced, which is highly compatible to such changes in the electrochemical kinetic behaviour.

Theoretical lithium storage mechanisms in TPPDA-NiPc materials were analyzed to elucidate structure-electrochemical performance relationships in COFs. (Fig. S4) The lithium storage mechanisms of the COFs include the lithium storage behavior by the redox of electroactive groups, the stepwise storage of lithium in the benzene ring, and the ion adsorption process occurring in the porous structure. Three different sets the redox peaks are observed in CV curves for TPPDA-NiPc materials, which reflect the three different steps of Li^+ insertion/extraction reactions, corresponding to different electrochemical redox reactions. Structural analysis indicate that unsaturated bonds (C=C, C=N, N=N) serve as primary Li^+ binding sites in COFs. Specifically, Li^+ interacts the C=N as well as N=N unsaturated groups on COF forming C-Li and N-Li. Processes which correspond with 2.60 V/2.23 V peaks from CV profile, and Li^+ undergo lithiation with macrocyclic conjugated structures in the phthalocyanine unit as well as with C=C in benzene ring, resulting in a peak of 0.96 V/0.88 V on CV profile. Additionally, COF network channels and interlayer voids participate in electrochemical reactions with Li^+, contributing to overall capacity. Nevertheless, the actual maximum capacity of the TPPDA-NiPc material is not clear enough due to buried redox reactive potentials due to agglomerate stacking in the COFs structure as well as the lithium storage behaviour of the porous structure while adsorbing ions. Collectively, theoretical mechanisms and electrochemical performance differences confirm that TPPDA-NiPc (1:2) possesses more accessible redox-active sites for Li^+ binding. It is further shown that with the increase of the proportion of phthalocyanine units, the degree of organic polymerization reaction is higher, and the network structure of TPPDA-NiPc (1:2) material is more complete and can provide more capacity.

In an attempt to further dissect and validate the lithium insertion/detachment mechanism in TPPDA-NiPc materials upon cycling, the three COFs electrodes were subjected to XPS fine C 1s, N 1s spectroscopy. C 1s spectrum for pristine TPPDA-NiPc (2:1) (Fig. 7a1) displayed five characteristic peaks at 283.43 eV (C=N), 284.19 eV (C=C), 285.45 eV (C-C), 287.72 eV (C-N), and 290.45 eV (π-π*conjugate structure). Upon discharge (Fig. 7a2), the C=C peak intensity (284.25 eV) decreased, whereas the C-C peak (284.74 eV) intensified markedly. Additionally, the peak corresponding to π-π conjugated structure no longer appeared while a new peak corresponding to C-Li (288.74 eV) was generated, which effectively proves that during discharge, C=C unsaturated functional units of COFs were disconnected as well as combined with Li^+ to form a C-Li bond. And after charging (Fig. 7a3), the peaks representing C=C showed a similar state

to the original polar sheet, and the peaks corresponding to the π-π conjugated structure reappeared. Simultaneously, there is a disappearance of the C-Li bond which is attributed by reconnection with a C=C bond in disconnected state during the charging process, which restores the conjugated structure, effectively proving that C=C in the material structure has good reversible lithium storage performance. The observed peak shifts and intensity variations originate from irreversible SEI formation reactions, accounting for the electrode's lower initial Coulombic efficiency. Analogously, C=N as well as C-N bonds undergo comparable transformations. The intensity of peak corresponding to C=N decreases while the intensity corresponding to the single bond is enhanced when lithium is embedded in the electrode material, Whereas intensity in the C=N peak was incompletely restored after removal of the lithium, which is mainly owing to some irreversible redox active spots in COF structure. Notably, analogous functional group transformations are evident in the C 1s spectra of TPPDA-NiPc (1:1) and (1:2) electrodes (Fig. 7b1-b3, c1-c3).

Given the participation of C=N bonds in electrochemical redox reactions, we examined the chemical state evolution of nitrogen-containing functional groups in TPPDA-NiPc electrodes during charge/discharge cycles. Five characteristic peaks were all present in the N 1s maps of the TPPDA-NiPc (2:1)/(1:1) electrodes (Fig. S5a,b), which were located at 398.5 eV (N=N), 399.4 eV (N=C), 400.3 eV (-NH2), 401.2 eV (N-C), and 406.1 eV (N-M, where M denotes metal ions). During discharge process, a characteristic peak at the TPPDA-NiPc (2:1)/(1:1) electrode located at about 399.4 eV was negatively displaced and weakened in intensity, while the peak at 401.2 eV was enhanced in intensity. This indicates Li^+ coordination with N=C bonds, forming N-C-Li structures during lithiation. Upon charging, the N=C and N-C peaks revert to their original states, consistent with reported N=C-involved lithium storage mechanisms. The N 1s spectrum of TPPDA-NiPc (1:2) (Fig. S5c) revealed analogous C=N and C-N transformations during cycling, confirming a comparable lithium (de)intercalation mechanism.

4. Conclusion

In this work, different ratios of phthalocyanine-based azo framework polymers (TPPDA-NiPc) were designed and synthesized by accurately regulating the molar ratios of TPPDA to nickel phthalocyanine (NiPc) (2:1, 1:1, and 1:2), and the effect of phthalocyanine content on framework structure and energy storage performance was systematically investigated. By increasing the proportion of NiPc monomer in the raw material, the network structure of the prepared TPPDA-NiPc material is more complete, the density of azo bonds is increased, the degree of polymerization is improved, and more reversible redox active sites are available in the framework network. Electrochemical characterization revealed the TPPDA-NiPc (1:2) electrode to possess optimal overall performance, improved cycling stability as well as rate capability when compared to (2:1) and (1:1). At 100 mA g^{-1} current density, TPPDA-NiPc (1:2) electrode exhibited capacity 970.5 mAh g^{-1} of reversible capacity, which is higher than the specific capacity of TPPDA-NiPc (2:1)/(1:1) material. Furthermore, rate capability evaluation demonstrated superior capacity retention for TPPDA-NiPc (1:2) across various current densities compared with the (2:1) and (1:1) variants. The superior electrochemical performance of TPPDA-NiPc (1:2) materials is explained by phthalocyanine's ability to promote formation within framework polymer network structures, improve the integrity of the framework network, and enhance the degree of organic polymerization, resulting in shortened ion transport paths and enhanced Li^+ kinetics. Tailoring the NiPc monomer ratio represents an effective strategy for optimizing azo-NiPc-COF polymerization behavior, offering a novel approach to the engineering of high-performance phthalocyanine-containing framework materials used in applications of energy.

Acknowledgments

The authors would like to express their sincere thanks to the National Natural Science Foundation of China (21762019 and 22463004), Natural Science Foundation of Jiangxi Province (20224ACB204004 and 20232BCJ22020), the Program of Qingjiang Excellent Young Talents in Jiangxi University of Science and Technology (JXUSTQJBJ2019003).

Conflict of Interest

The authors declare no competing financial interest.

Supporting information

Applicable.

CRediT Statement

Danlin Sun: experiments, data curation, original draft preparation, manuscript writing. **Suqin Liu:** experiments, data curation, electrochemical performance, tests original draft preparation. **Gaoyou Du:** investigation, formal analysis, grammatical modification and polish. **Qiong Luo:** methodology, investigation, data analysis and processing. **Renjie Peng:** methodology, investigation, methodology. **Jun Chen:** conceptualization, manuscript revision, supervision, funding acquisition.

References

[1] S. Li, K. Wang, G. Zhang, S. Li, Y. Xu, X. Zhang, X. Zhang, S. Zheng, X. Sun, Y. Ma, Fast charging anode materials for lithium-ion batteries: current status and perspectives, *Advanced Functional Materials*, 2022, **32**, 2200796, doi: 10.1002/adfm.202200796.

[2] Lyu, Y.; Wu, X.; Wang, K.; Feng, Z.; Cheng, T.; Liu, Y.; Wang, M.; Chen, R.; Xu, L.; Zhou, J.; et al. An Overview on the Advances of $LiCoO_2$ Cathodes for Lithium-Ion Batteries, *Advanced Energy Materials,* 2021, **11**(2), 2000982, doi: 10.1002/aenm.202000982

[3] Xu, D.; Liang, M.; Qi, S.; Sun, W.; Lv, L.-P.; Du, F.-H.; Wang,

B.; Chen, S.; Wang, Y.; Yu, Y. The Progress and Prospect of Tunable Organic Molecules for Organic Lithium-Ion Batteries, *ACS Nano*, 2021, **15** (1), 47-80, doi: 10.1021/acsnano.0c05896

[4] Jin, Y.; Zhang, T.; Zhang, M. Advances in Intelligent Regeneration of Cathode Materials for Sustainable Lithium-Ion Batteries. *Advanced Energy Materials*, 2022, **12** (36), 2201526, doi: 10.1021/acsnano.0c05896

[5]Reddy, R. C. K.; Lin, J.; Chen, Y.; Zeng, C.; Lin, X.; Cai, Y.; Su, C.-Y. Progress of nanostructured metal oxides derived from metal–organic frameworks as anode materials for lithium–ion batteries, *Coordination Chemistry Reviews*, 2020, **420**, 213434, doi:10.1016/j.ccr.2020.213434

[6] M. Wang, Y. Song, W. Wei, H. Liang, Y. Yi, X. Wang, D. Ren, L. Wang, J. Wang, Y. Wei, X. He, Y. Yang, First fluorescent probe for graphite anodes of lithium-ion battery, *Matter*, 2023, **6**, 873-886, doi: 10.1016/j.matt.2022.12.014.

[7] S. Luo, F. Liu, W. Tianxu, Y. Liu, C. Zhang, C. Bie, M. Liu, P. K. Chu, K. Huo, B. Gao, Regeneration of spent graphite *via* graphite-like turbostratic carbon coating for advanced Li ion battery anode, *Energy Storage Materials*, 2024, **73**, 103833, doi: 10.1016/j.ensm.2024.103833.

[8] Y. Liu, H. Shi, Z.-S. Wu, Recent status, key strategies and challenging perspectives of fast-charging graphite anodes for lithium-ion batteries, *Energy & Environmental Science*, 2023, **16**, 4834-4871, doi: 10.1039/D3EE02213G.

[9] L. Sun, Y. Liu, L. Wang, Z. Jin, Advances and future prospects of micro-silicon anodes for high-energy-density lithium-ion batteries: a comprehensive review, *Advanced Functional Materials*, 2024, **34**, 2403032, doi: 10.1002/adfm.202403032.

[10] R. Amine, A. Daali, X. Zhou, X. Liu, Y. Liu, Y. Ren, X. Zhang, L. Zhu, S. Al-Hallaj, Z. Chen, G.-L. Xu, K. Amine, A practical phosphorus-based anode material for high-energy lithium-ion batteries, *Nano Energy*, 2020, **74**, 104849, doi: 10.1016/j.nanoen.2020.104849.

[11] G. Xie, X. Tan, Z. Shi, Y. Peng, Y. Ma, Y. Zhong, F. Wang, J. He, Z. Zhu, X.-B. Cheng, G. Wang, T. Wang, Y. Wu, SiO_x based anodes for advanced Li-ion batteries: recent progress and perspectives, *Advanced Functional Materials*, 2025, **35**, 2414714, doi: 10.1002/adfm.202414714.

[12] M. Han, K. Zheng, J. Liu, Z. Zou, Y. Mu, H. Hu, F. Yu, W. Li, L. Wei, L. Zeng, T. Zhao, Mechanistic insights into capacity discrepancies of conversion-type transition-metal compounds in wide-temperature-range lithium-ion batteries, *Journal of Materials Chemistry A*, 2025, **13**, 1086-1094, doi: 10.1039/D4TA06381C.

[13] K.-H. Nam, S. Jeong, B.-C. Yu, J.-H. Choi, K.-J. Jeon, C.-M. Park, Li-compound anodes: a classification for high-performance Li-ion battery anodes, *ACS Nano*, 2022, **16**, 13704-13714, doi: 10.1021/acsnano.2c05172.

[14] Y. Wu, H. Ye, Y. Li, Molecular engineering of organic electrode materials for beyond lithium-ion batteries, *Advanced Functional Materials*, 2025, **35**, 2424329, doi: 10.1002/adfm.202424329.

[15] X. Wu, W. Zhou, C. Ye, J. Zhang, Z. Liu, C. Yang, J. Peng, J. Liu, P. Gao, Porphyrin-thiophene based conjugated polymer cathode with high capacity for lithium-organic batteries, *Angewandte Chemie (International Ed)*, 2024, **63**, e202317135, doi: 10.1002/anie.202317135.

[16] J. Huang, X. Dong, Z. Guo, Y. Wang, Progress of organic electrodes in aqueous electrolyte for energy storage and conversion, *Angewandte Chemie (International Ed)*, 2020, **59**, 18322-18333, doi: 10.1002/anie.202003198.

[17] Y. Lu, J. Chen, Prospects of organic electrode materials for practical lithium batteries, *Nature Reviews Chemistry*, 2020, **4**, 127-142, doi: 10.1038/s41570-020-0160-9.

[18] H.-G. Wang, Q. Wu, L. Cheng, L. Chen, M. Li, G. Zhu, Porphyrin- and phthalocyanine-based systems for rechargeable batteries, *Energy Storage Materials*, 2022, **52**, 495-513, doi: 10.1016/j.ensm.2022.08.022.

[19] L. Yu, X. Chen, N. Yao, Y.-C. Gao, Y.-H. Yuan, Y.-B. Gao, C. Tang, Q. Zhang, Advanced carbon as emerging energy materials in lithium batteries: A theoretical perspective, *InfoMat*, 2025, **7**, e12653, doi: 10.1002/inf2.12653.

[20] Z. Wang, H. Jiang, Y. Zhang, Y. An, C. Wei, L. Tan, S. Xiong, Y. Qian, J. Feng, Application of 2D MXene in organic electrode materials for rechargeable batteries: recent progress and perspectives, *Advanced Functional Materials*, 2023, **33**, 2210184, doi: 10.1002/adfm.202210184.

[21] D. Zhu, G. Xu, M. Barnes, Y. Li, C.-P. Tseng, Z. Zhang, J.-J. Zhang, Y. Zhu, S. Khalil, M. M. Rahman, R. Verduzco, P. M. Ajayan, Covalent organic frameworks for batteries, *Advanced Functional Materials*, 2021, **31**, 2100505, doi: 10.1002/adfm.202100505.

[22] J. Zhou, B. Zheng, X. Huang, W. Zhou, C. Sun, X. Sun, T. Zhang, Z. Huang, S. Tan, J. Liu, P. Gao, High voltage, long cycling organic cathodes rendered by *in situ* electrochemical oxidation polymerization, *Advanced Functional Materials*, 2024, **34**, 2411127, doi: 10.1002/adfm.202411127.

[23] L. Zhou, S. Jo, M. Park, L. Fang, K. Zhang, Y. Fan, Z. Hao, Y.-M. Kang, Structural engineering of covalent organic frameworks for rechargeable batteries, *Advanced Energy Materials*, 2021, **11**, 2003054, doi: 10.1002/aenm.202003054.

[24] C. Wang, Z. Zhang, Y. Zhu, C. Yang, J. Wu, W. Hu, 2D covalent organic frameworks: from synthetic strategies to advanced optical-electrical-magnetic functionalities, *Advanced Materials*, 2022, **34**, e2102290, doi: 10.1002/adma.202102290.

[25] J. Zou, K. Fan, Y. Chen, W. Hu, C. Wang, Perspectives of ionic covalent organic frameworks for rechargeable batteries, *Coordination Chemistry Reviews*, 2022, **458**, 214431, doi: 10.1016/j.ccr.2022.214431.

[26] C. Zhang, F. Li, T. Gu, X. Song, J. Yuan, L. Ouyang, M. Zhu, J. Liu, Covalent organic frameworks for high-performance rechargeable lithium metal batteries: Strategy, mechanism, and application, *Progress in Materials Science*, 2025, **152**, 101455, doi: 10.1016/j.pmatsci.2025.101455.

[27] M. S. Lohse, T. Bein, Covalent organic frameworks: covalent organic frameworks: structures, synthesis, and applications, *Advanced Functional Materials*, 2023, **28**(33) doi:10.1002/adfm.201705553

[28] Y. Yusran, Q. Fang, V. Valtchev, Electroactive covalent

organic frameworks: design, synthesis, and applications, *Advanced Materials*, 2020, **32**, e2002038, doi: 10.1002/adma.202002038.
[29] J. Zhao, M. Zhou, J. Chen, L. Wang, Q. Zhang, S. Zhong, H. Xie, Y. Li, Two birds one stone: graphene assisted reaction kinetics and ionic conductivity in phthalocyanine-based covalent organic framework anodes for lithium-ion batteries, *Small*, 2023, **19**, 2303353, doi: 10.1002/smll.202303353.
[30] Q. Liu, Q. Li, Y. Li, T. Su, B. Hou, Y. Zhao, Y. Xu, Two-dimensional covalent organic frameworks in organic electronics, *Angewandte Chemie (International Ed)*, 2025, **64**, e202502536, doi: 10.1002/anie.202502536.
[31] L. Zhu, Y. Cao, T. Xu, H. Yang, L. Wang, L. Dai, F. Pan, C. Chen, C. Si, Covalent organic framework membranes for energy storage and conversion, *Energy & Environmental Science*, 2025, **18**, 5675-5739, doi: 10.1039/D5EE00494B.
[32] J. Á. Martín-Illán, D. Rodríguez-San-Miguel, F. Zamora, Evolution of covalent organic frameworks: from design to real-world applications, *Coordination Chemistry Reviews*, 2023, **495**, 215342, doi: 10.1016/j.ccr.2023.215342.
[33] Q. Li, Y. Zhu, T. Pan, G. Zhang, H. Pang, Covalent organic framework nanomaterials: Syntheses, architectures, and applications, *Advances in Colloid and Interface Science*, 2025, **339**, 103427, doi: 10.1016/j.cis.2025.103427.
[34] K. Li, P. Wang, J. Li, Y. Gao, Y. Zhang, Boosting oxygen reduction reaction with metal phthalocyanines: altering central metals and substituents, *Journal of Materials Chemistry A*, 2024, 12, 25918-25926, doi: 10.1039/D4TA04816D.
[35] Y. Zang, P. Peng, F. Pei, R.-H. Li, L. Wu, D.-Q. Lu, Y. Zhang, K. Huang, Y. Shen, Y.-H. Huang, Y.-Q. Lan, Conjugated phthalocyanine-based framework as artificial SEI for over 400 Wh kg^{-1} lithium-metal battery, *National Science Review*, 2024, **12**, nwae443, doi: 10.1093/nsr/nwae443.
[36] R. Jiang, X. Wang, Q. Zhi, Z. Liu, X. Yang, C. Li, Q. Xu, X. Zhan, K. Wang, L. Zhang, J. Jiang, Y. Feng, Conjugated phthalocyanine-based mesoporous covalent organic frameworks for efficient anodic lithium storage, *Small*, 2025, **21**, e2410405, doi: 10.1002/smll.202410405.
[37] S. Liu, L. Wang, L. Li, Q. Luo, J. Chen, Chemically exfoliated few-layer phthalocyanine-based covalent organic frameworks used as improved energy storage electrode for lithium-ion batteries, *Journal of Energy Storage*, 2024, **98**, 113124, doi: 10.1016/j.est.2024.113124.
[38] Y. Zhang, X. Zhang, L. Jiao, Z. Meng, H.-L. Jiang, Conductive covalent organic frameworks of polymetallophthalocyanines as a tunable platform for electrocatalysis, *Journal of the American Chemical Society*, 2023, **145**, 24230-24239, doi: 10.1021/jacs.3c08594.
[39] Y. Yue, P. Cai, K. Xu, H. Li, H. Chen, H.-C. Zhou, N. Huang, Stable bimetallic polyphthalocyanine covalent organic frameworks as superior electrocatalysts, *Journal of the American Chemical Society*, 2021, **143**, 18052-18060, doi: 10.1021/jacs.1c06238.
[40] C. Luo, W. University, Y. Zhou, W. University, Y. Guo, W. University, X. Li, W. University, R. Li, W. University, T. Peng, W. University, Cobalt phthalocyanine-based covalent organic framework with bimetallic synergistic effect for efficient photocatalytic CO_2 reduction, *ACS Sustainable Chemistry & Engineering*, 2024, **12**, 18691-18703, doi: 10.1021/acssuschemeng.4c08044.
[41] J. Zhao, M. Zhou, J. Chen, L. Tao, Q. Zhang, Z. Li, S. Zhong, H. Fu, H. Wang, L. Wu, Phthalocyanine-based covalent organic frameworks as novel anode materials for high-performance lithium-ion/sodium-ion batteries, *Chemical Engineering Journal*, 2021, **425**, 131630, doi: 10.1016/j.cej.2021.131630.
[42] H. Kong, Y. Guan, J. Wang, W. Sun, L. Chen, J. Ou, L. Xie, F. Fu, H. Zhang, H. Chen, An intercalation–conversion hybrid mechanism enables covalent organic frameworks with superior Li-ion storage, *Journal of Materials Chemistry A*, 2022, **10**, 20866-20873, doi: 10.1039/D2TA05871E.
[43] D. Luo, H. Zhao, F. Liu, H. Xu, X. Dong, B. Ding, H. Dou, X. Zhang, Outstanding lithium storage performance of a copper-coordinated metal-covalent organic framework as anode material for lithium-ion batteries, *Energy & Environmental Materials*, 2024, **7**, e12732, doi: 10.1002/eem2.12732.
[44] J. Zhao, M. Zhou, J. Chen, L. Wang, Q. Zhang, S. Zhong, H. Xie, Y. Li, Two birds one stone: graphene assisted reaction kinetics and ionic conductivity in phthalocyanine-based covalent organic framework anodes for lithium-ion batteries, *Small*, 2023, **19**, 2303353, doi: 10.1002/smll.202303353.
[45] C. Choi, D. S. Ashby, D. M. Butts, R. H. DeBlock, Q. Wei, J. Lau, B. Dunn, Achieving high energy density and high power density with pseudocapacitive materials, *Nature Reviews Materials*, 2020, **5**, 5-19, doi: 10.1038/s41578-019-0142-z.